# Kalman Tracking and Bayesian Detection for RADAR RFI Blanking

Weizhen Dong, Brian D. Jeffs,
Department of Electrical and Computer Engineering, Brigham Young University, Provo, UT 84606;
wzhdong@hotmail.com, bjeffs@ee.byu.edu
and
J. Richard Fisher
National Radio Astronomy Observatory, 520 Edgemont Road, Charlottesville, VA 22903-2524;
rfisher@gb.nrao.edu

***Abstract*— L-Band observations at the Green Bank Telescope (GBT) and other radio observatories are plagued with interference from pulsed aviation RADAR transmissions. One remaining problem is that even when strong direct path pulses and nearby fixed clutter echoes are removed, there are still weaker aircraft echoes present which can corrupt the data. In this paper we present an algorithm which improves aircraft echo blanking by forming a Kalman filter tracker to follow the path of a sequence of echoes observed on successive RADAR antenna sweeps. The tracks developed for each aircraft can be used to predict regions (in bearing and range) for the next expected echoes, even before they are detected. The data in these regions can then be blanked in real time without waiting for the pulse peak to arrive. Additionally, we present a new Bayesian algorithm which combines tracker and pulse detector operations to enable more sensitive weak pulse acquisition. The developed track information is used to form a spatial prior probability distribution for the presence of the next echoes. Regions with higher probability are processed with a lower detection threshold to pull out low level pulses without increasing the overall probability of false alarm detection.**

***Index Terms*— RFI mitigation, Kalman tracking, Bayesian detection, radio astronomy.**

## I. Introduction

RADIO astronomical observation is polluted by a wide range of radio frequency interference (RFI). Astronomers and engineers are facing unprecedented challenges as they attempt to solve the problem of RFI mitigation.

For example, air surveillance RADAR transmissions such as those from the ARSR-3 system occur in the important red shifted Hydrogen line observation frequency range from 960-1400 MHz. These signals may dramatically disturb radio astronomical observations, and have been reported to be a significant problem at the Green Bank Telescope (GBT) [1] [2] [3], Arecibo [4] [5], and other observatories . However, the induced pollution is impulsive and transient, so for radio astronomy observation, one solution is to "time-blank" by simply not including RADAR-pulse-corrupted data samples during spectrum estimation [6] [1]. Time blanking has also been used to mitigate interference from mobile wireless communications services [7] [8] [9]. It has also been proposed that once detected, RADAR pulses can be removed by parametric signal subtraction without discarding data [5].

This work is supported by the National Scicence Foundation grant number AST-9987339

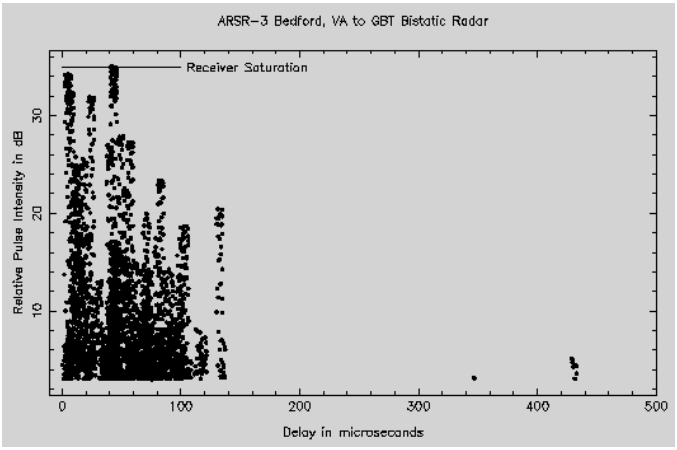


Fig. 1. Pulse intensity as a function of delay from the directly arriving pulse

To illustrate the interference problem addressed in this paper, we present some 1292 MHz data recorded at the GBT which clearly shows the interfering RADAR signal. Some valuable analysis of this real-world data is provided in [2][3]. Figure 1 shows pulse intensity as a function of delay relative to the first arriving pulse. Strong pulses can be seen out to a delay of 135

microseconds, most of which are due to reflections from the hilly terrain around the GBT. These can typically be excised using time window blanking. The group of returns at 430 microseconds is from an aircraft, and blanking it is more problematical since it is not present at this same location during each successive transmit antenna sweep.

There are two approaches to time-blanking which we will call respectively, "time window blanking" and "detected pulse blanking." Strong direct-path pulses and nearby fixed terrain clutter echoes have a predictable repetition cycle and can be removed by simple time window blanking. In this approach a fixed set of time intervals, synchronized to the RADAR pulse repetition rate, are removed from the data during each transmit antenna sweep cycle. However, aircraft echoes arrive at arbitrary times due to aircraft motion, and thus must be detected before they can be blanked. Detected pulse blanking is used in this case to remove a window of data surrounding each detected aircraft echo, including transmit antenna beampattern sidelobes.

Two difficulties arise with detected pulse blanking:

1) It is very hard to perform blanking in real time because echoes include wide sidelobe patterns from the RADAR transmit beampattern (seen Figure 2). For real-time operation the echo must be anticipated and the full beam sidelobe structure must be removed before and after the echo peak arrives.
2) Echoes weak enough to make detection of even the peak amplitude difficult may still cause significant corruption to the data set.

This paper presents improved methods for detected pulse blanking based on Kalman filter tracking of aircraft echo motion. The proposed algorithm utilizes time-history information across multiple past RADAR antenna sweeps to predict the location of detections in the next upcoming transmit antenna pass. This prediction is used either to form a real-time blanking region around an anticipated echo peak, or to form a prior probability distribution for pulse arrivals. This prior distribution can be used in a Bayesian framework to improve weak echo detection.

We will focus on implementation of the Kalman tracker and predictive real-time blanking for real RADAR interference data recorded at the GBT. An improved Bayesian detection scheme using track-based echo prior probabilities will be briefly introduced here, and more fully developed in a following paper.

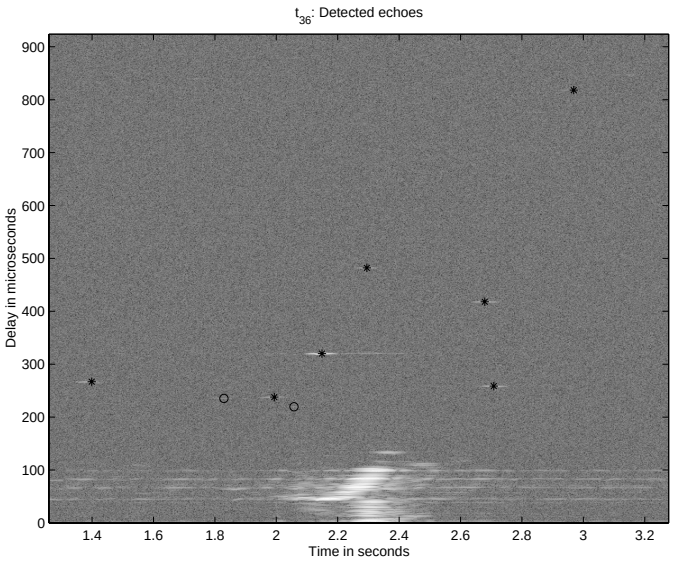


Fig. 2. Typical RADAR sweep time frame as seen at the GBT. Coarse horizontal axis time index corresponds to bearing angle at transmit antenna. Vertical axis is two-way bistatic pulse echo time from transmitter to GBT, yielding aircraft range. Each column of pixels corresponds to a single transmitted pulse. Bright regions up to 120 $\mu$s are fixed echoes from nearby mountainous terrain. Note the wide transmit antenna sidelobe pattern for the echo at 310 $\mu$s delay. Automatically detected aircraft echoes are marked. Echoes detected using a constant threshold $T_0$ are represented by stars, and notes there are two weaker echoes are miss-detected in the circle positions, but were found by the Bayesian detection scheme without increasing false alarm rate.

## II. Kalman Tracking for Interfering Aircraft Echoes

This section presents details of the tracker implementation. A classical Kalman filter approach as often used for RADAR target following was implemented with some modifications [10] [11] [12]. State equations for aircraft dynamics are represented in Cartesian, $x - y$, coordinates and are thus non-linearly related to the natural polar (range and bearing) coordinate system of the RADAR detector. This mismatch necessitates use of an extended Kalman filter implementation to liniarize the observation data points. Also, in the RFI case we have a "bistatic" RADAR scenario where the transmitter and receiver are widely separated. The ARSR-3 signals seen at the GBT originate This geometry complicates estimating true range and bearing. However, since the goal is not to precisely localize each aircraft in real-world coordinates, but to build a predictive tracker in any suitable coordinate system, we make no attempt to estimate actual range and bearing relative to the GBT.

The CLEAN algorithm [13] provides isolated detections in range and bearing, $\boldsymbol{z}_n = [r_n, \theta_n]^T$, for each RADAR antenna sweep. These detections serve as inputs to the tracker. Here $n$ is the antenna sweep, "snapshot"

index for time $t_n$. Also for notational simplicity we focus on detections from a single track. The desired tracker outputs at snapshot $n$ are a prediction point, $(\hat{x}_{n+1|n}, \hat{y}_{n+1|n})$, where the next detection is expected, and shape parameters for an elliptical uncertainty region, $\mathcal{S}_{n+1}$, centered on this point (see Figure 3). The size of $\mathcal{S}_{n+1}$ depends on the quality of the track, and gets larger with an increase in observation noise, missed snapshot detections, or rapid acceleration of the target. $\mathcal{S}_{n+1}$ selects the region for predictive real-time blanking, or the region of increased prior probability for an arriving echo pulse for the detection step in snapshot $n+1$.

### A. Dynamic and Observation Models

The tracker employs a position-and-velocity state space model to describe the dynamics of motion for the aircraft. Constant velocity motion perturbed by a correlated zero mean Gaussian random acceleration, $\boldsymbol{a}_n$, is assumed. Measurements are obtained at discrete sample "snapshot" times, $t_n$, separated by intervals of $T$ seconds. The dynamic motion model is

$$\begin{aligned} \boldsymbol{x}_{n+1} &= \boldsymbol{F}\boldsymbol{x}_n + \boldsymbol{G}\boldsymbol{a}_n, \text{ where} \\ \boldsymbol{x}_n &= \begin{bmatrix} x_n & y_n & \dot{x}_n & \dot{y}_n \end{bmatrix}^T, \\ \boldsymbol{F} &= \begin{bmatrix} 1 & 0 & T & 0 \\ 0 & 1 & 0 & T \\ 0 & 0 & 1 & 0 \\ 0 & 0 & 0 & 1 \end{bmatrix}, \\ \boldsymbol{G} &= \begin{bmatrix} \frac{T^2}{2} & 0 & T & 0 \\ 0 & \frac{T^2}{2} & 0 & T \end{bmatrix}^T, \end{aligned} \tag{1}$$

where $\boldsymbol{x}_n$ is the state vector for a single aircraft, $x_n$ and $\dot{x}_n$ represent position and velocity respectively in the $x$ direction, $\boldsymbol{F}$ is the state transition matrix, and $\boldsymbol{G}$ is the input distribution matrix.

The measurement model relates polar observations, $\boldsymbol{z}_n$, to the state equation coordinates and includes observation measurement noise:

$$\begin{aligned} \boldsymbol{z}_n &= \boldsymbol{h}(\boldsymbol{x}_n) + \boldsymbol{v}_n, \text{ where} \\ \boldsymbol{h}(\boldsymbol{x}_n) &= \begin{bmatrix} \sqrt{x_n^2 + y_n^2} \\ \tan^{-1} \frac{y_n}{x_n} \end{bmatrix}, \\ \boldsymbol{v}_n &= [v_r(n), v_\theta(n)]^T, \end{aligned} \tag{2}$$

$r_n$ and $\theta_n$ are the measured range and bearing respectively at snapshot $n$, with corresponding measurement noise $v_r(n)$ and $v_\theta(n)$.

### B. Kalman Prediction Equations

Given echo detections and associated track history up to snapshot $n$, the first step in a Kalman filter iteration is to predict the next state vector and update the prediction error covariance estimate as follows:

$$\hat{\boldsymbol{x}}(n+1|n) = \boldsymbol{F}\hat{\boldsymbol{x}}(n|n), \tag{3}$$

$$\boldsymbol{P}(n+1|n) = \boldsymbol{F}\boldsymbol{P}(n|n)\boldsymbol{F} + \boldsymbol{G}\boldsymbol{Q}\boldsymbol{G}, \tag{4}$$

where

$$\begin{aligned} \hat{\boldsymbol{x}}(n|n) &= \text{filtered state estimate at } t_n \\ &\quad \text{given data through } t_n, \\ \boldsymbol{P}(n|n) &= \text{filtered state error covariance,} \\ \hat{\boldsymbol{x}}(n+1|n) &= \text{predicted state estimate,} \\ \boldsymbol{P}(n+1|n) &= \text{predicted state error covariance,} \\ \boldsymbol{Q} &= \text{process noise/acceleration covariance.} \end{aligned}$$

$\hat{\boldsymbol{x}}(n|n)$ and $\boldsymbol{P}(n|n)$ are computed using filter equations, (6)–(8), presented in Section II-C. Note that the prediction point, $(\hat{x}_{n+1|n}, \hat{y}_{n+1|n})$, is given by the first two elements of $\hat{\boldsymbol{x}}(n+1|n)$. We define the elliptical region, $\mathcal{S}_{n+1}$ to be centered on this point and to have radii $r_x$ and $r_y$ proportional to $\sqrt{\boldsymbol{P}_{1,1}(n+1|n)}$ and $\sqrt{\boldsymbol{P}_{2,2}(n+1|n)}$ respectively. Thus the larger the prediction error variance, the larger $\mathcal{S}_{n+1}$ grows to represent our uncertainty as to where the next RADAR echo will be detected.

Figure 3 illustrates this behavior. The plot shows track evolution for real GBT data over five snapshots for a dense scene with multiple, overlapping aircraft tracks. The ellipses show prediction regions, $\mathcal{S}_{n+1}$ for each established track. Note the variety of sizes, corresponding to variations in track quality. For real-time processing, these prediction regions would be blanked for the next expected echoes, even before they are detected. However for post processing, the prior information represented by these ellipses can be used for a Bayesian combined tracking-with-detection algorithm to improve sensitivity to weak pulses.

Two successive associated pulse detections are required before a track can be initiated. $\hat{\boldsymbol{x}}(0|0)$ is initialized with the position of the second detection, and a two sample velocity estimate computed from the position difference between the detections.

To find a practical initialization for $\boldsymbol{P}(0|0)$, we ran the tracker on synthetic detection data which simulated the aircraft motion seen in the real GBT data. After a large number of Monte Carlo random trials, $\boldsymbol{P}(n|n)$ converged on average to $\boldsymbol{P}(\infty|\infty) \approx (2 \times 10^3)\boldsymbol{I}$. This value was used to initialize $\boldsymbol{P}(0|0)$ when processing real data from GBT.

In simulation, $\boldsymbol{a}_n = [a_x(n), a_y(n)]^T$ was generated by lowpass filtering two mutually independent Gaussian white noise time sequences (one each for $a_x(n)$ and

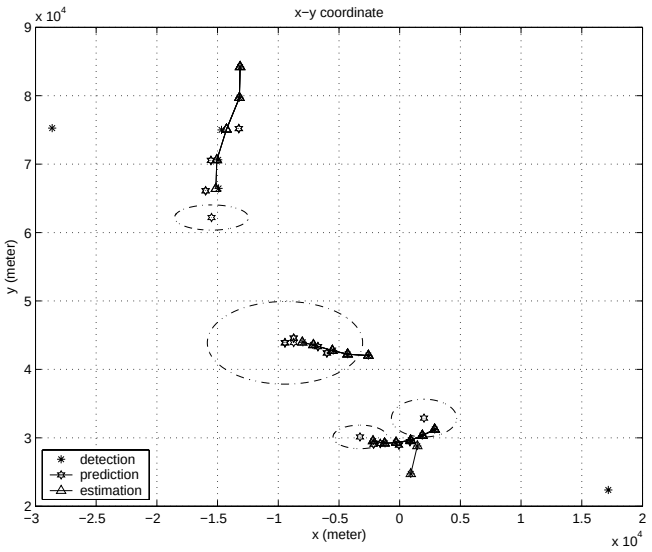


Fig. 3. An example of Kalman tracking performance for data acquired at the GBT. Four aircraft tracks have been automatically established and plotted, including a pair of crossing tracks. Data from five snapshots is shown with $T \approx 24$s. The final point plotted for each track in the prediction point, $(\hat{x}_{n+1|n}, \hat{y}_{n+1|n})$. Prediction regions, $\mathcal{S}_{n+1}$, shown by the dashed ellipses vary in size according to track quality. Note that the center track has a large $\mathcal{S}_{n+1}$ due to a missed detection. Predictive real-time blanking is accomplished by excising the prediction region data.

$a_x(n)$). A filter cutoff of $f_c = \frac{1}{100T}$ produced smooth simulated aircraft turning maneuvers which were consistent with tracks seen in the real GBT data. The process covariance is modeled as a constant matrix of the form

$$\boldsymbol{Q} = E\{\boldsymbol{a}_n \boldsymbol{a}_n^T\} = \begin{bmatrix} \sigma_x^2 & \sigma_{xy}^2 \\ \sigma_{xy}^2 & \sigma_y^2 \end{bmatrix}. \tag{5}$$

Values of $\sigma_x^2 = \sigma_y^2 = 12.0$ and $\sigma_{xy}^2 = \sigma_{yx}^2 = 0$ were used in the results described below and were established by qualitatively matching simulated tracks with the real GBT data.

### C. Kalman Update (Filter) Equations

When a new snapshot of detections from CLEAN is available, the Kalman update step completes the iteration begun with equations (3) and (4) as follows:

$$\hat{\boldsymbol{x}}(n+1|n+1) = \hat{\boldsymbol{x}}(n+1|n) + \boldsymbol{K}(n+1) \times \left[\boldsymbol{z}(n+1) - \boldsymbol{h}\Big(\hat{\boldsymbol{x}}(n+1|n)\Big)\right], \tag{6}$$

$$\boldsymbol{P}(n+1|n+1) = \Big[\boldsymbol{I} - \boldsymbol{K}(n+1)\boldsymbol{H}(n+1)\Big] \times \boldsymbol{P}(n+1|n), \tag{7}$$

$$\boldsymbol{K}(n+1) = \boldsymbol{P}(n+1|n)\boldsymbol{H}^T(n+1) \times \big[\boldsymbol{H}(n+1)\boldsymbol{P}(n+1|n)\boldsymbol{H}^T(n+1) + \boldsymbol{R}\big]^{-1}, \tag{8}$$

where

$$\boldsymbol{H}(n+1) \stackrel{\triangle}{=} \left[\frac{\partial h}{\partial \boldsymbol{x}}\right]_{\boldsymbol{x}=\hat{\boldsymbol{x}}(n+1|n)} = \left(\frac{1}{\sqrt{x^2(n+1|n) + y^2(n+1|n)}}\right) \times \begin{bmatrix} x(n+1|n) & y(n+1|n) & 0 & 0 \\ -y(n+1|n) & x(n+1|n) & 0 & 0 \end{bmatrix}, \tag{9}$$

and where $\boldsymbol{K}(n+1)$ is the Kalman gain matrix. Range and bearing measurement noise are assumed to be mutually independent, so the measurement error covariance, $\boldsymbol{R}$, has form

$$\boldsymbol{R} = \begin{bmatrix} \sigma_r^2 & 0 \\ 0 & \sigma_\theta^2 \end{bmatrix}. \tag{10}$$

$\sigma_r^2$ is proportional to receiver noise variance and the square of transmit pulse length. $\sigma_\theta^2$ is proportional noise and the square of transmit antenna angular rotation rate divided by transmit pulse repetition rate. We have estimated these parameters empirically for the GBT data and treat them as constants in the Kalman update.

After computing (6), (7), and (8), index $n$ is incremented to complete the iteration which started with prediction equations (3) and (4).

### D. Track Management

In practical multiple target automatic tracking applications it is necessary to deal with a number of ambiguities when interpreting the pulse detection data. We have developed a set of rule–based procedures (more fully described in [14]) to address the following issues.

1) *Track Creation and Association.* For each new snapshot the CLEAN algorithm produces a set of detections. Each of these must be classified as being a newly detected aircraft for which a track must be created, or as belonging to an existing track. Detections which lie within a fixed distance, $d_a$, from an existing track's prediction point, $(\hat{x}_{n+1|n}, \hat{y}_{n+1|n})$, are associated with that track. To avoid ambiguities, detections which satisfy this criterion for two or more distinct tracks are assigned to the track whose prediction point is closest.
Two successive associated detections are required to start a track. New detections which are not within a distance $d_a$ of any existing prediction point are designated candidate starting points. The track is created if in the succeeding snapshot a detection within distance $d_n$ of the candidate point is found which is not associated with any existing track. Since no velocity information is available

from a single candidate point, it is necessary that $d_n >> d_a$. In practice $d_n$ is set to be the maximum distance an aircraft can travel in $T$ seconds.

2) *Missed Detections.* If in a given snapshot no new detection is associated with a particular track, it is assumed that the aircraft is still present, but that the detection was missed due to random variation in echo amplitude. Consider missing $k$ successive detections for a given track. In this case, Kalman prediction equations (1), (3), and (4) from prior snapshot, $t_{n-k}$, are recomputed as a multi–step prediction by replacing $T$ with $kT$. This produces the desired $k$–step prediction point $(\hat{x}_{n+1|n-k}, \hat{y}_{n+1|n-k})$ but the prediction error covariance, $\boldsymbol{P}(n+1|n-k)$ increases, and the size of $\mathcal{S}_{n+1}$ grows as compared to a normal single step prediction.
3) *Track Dropping.* A track which has no associated detections in three successive snapshots is terminated.
4) *Track Splitting.* If two or more new detections are associated with a single track then the track is split into separate tracks for each new detection. These split tracks have a common history for $t \leq t_{n-1}$ but for $t \geq t_n$ are computed as distinct tracks. This scenario arises when aircraft paths cross or when a new aircraft detection occurs close to an existing track prediction point.

## III. A Bayesian Combined Kalman Tracker and Detector

In a conventional RADAR detector, all range-bearing bins are assumed to be equally likely to contain an echo. Detections are made when the magnitude–squared matched filter output exceeds a predetermined constant threshold, $\tau$.[1] Thresholds are set to yield a specified probability of false alarm (PFA). For a fixed PFA, the probability of detection (PD) is a function of the receiver design and signal statistics, such as signal to noise ratio.

In the context of the Kalman tracker, one need not assume all bins have the same probability of detection. The track histories provide prior information which indicates a higher probability of echoes being detected in prediction regions, $\mathcal{S}_{n+1}$. We propose a Bayesian detection scheme where a spatially dependent prior probability density function for the presence of an echo, $p(x, y)$, is computed using the $\mathcal{S}_{n+1}$ ellipses to designate areas of increased density. With this approach it is possible to increase the overall PD without an increase in PFA. A detailed theoretical development of this detector is found in [14] and in a forthcoming paper. Here it is simply noted in summary that the effect of the Bayesian detector is to make the detection threshold, $\tau(x, y)$ spatially varying, with local minima at the prediction point centroids of the $\mathcal{S}_{n+1}$ regions, as illustrated in Figure 4. Section IV presents a comparison of spectral density estimates with conventional and the proposed Bayesian detectors. The proposed scheme produces less RADAR pulse bias in the spectral estimate.

[1]The widely used constant false alarm rate (CFAR) detector scales a constant, $c$, by a local estimate of noise and clutter standard deviation in order to form a variable threshold, $\tau(r, \theta)$. The Bayesian detection process described here can still be applied to $c$ to achieve the claimed effect.

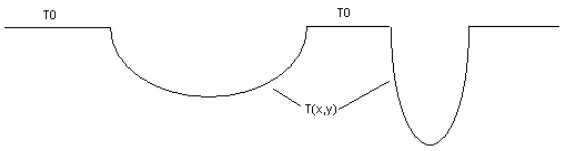


Fig. 4. The threshold $\tau$ is determined by the prior distribution $p(x, y)$ of the presence of pulse. $\tau_0$ is the constant threshold outside the elliptical regions, $\mathcal{S}_{n+1}$. $\tau(x, y)$ is at a local minimum corresponding to each prediction point. The two concavities represent decreased threshold according to the prior probability inside two different sized $\mathcal{S}_{n+1}$.

## IV. Experimental Results

A set of real data recorded at the GBT for a 10 MHz wide band around 1292 MHz was used to test the echo detection algorithm, tracking, and blanking performance. A sequence of files representing a continuous block of 10 minutes of data (50 RADAR antenna rotations) was recorded in January, 2003. By using the tracker information, the new Bayesian algorithm is able to detect some weaker echoes which are miss-detected by the conventional method. This was accomplished without increasing the false alarm rate significantly. All blanking was implemented by "zero-stuffing" [1], that is, placing zeros into the time samples where RADAR interference is detected.

The ability to excise RADAR interference was evaluated for three different blanking techniques: 1) simple time window blanking, 2) combined time window and detected pulse blanking using conventional pulse detection, and 3) combined time window and detected pulse blanking using the proposed Bayesian detector. The Kalman tracker was used for both detected pulse blanking methods.

Figure 5 shows the unblanked spectrum accumulated over a 1.2 second window which contained terrain echo clutter and aircraft echoes. Note the dominant spectral peak around 5.5 MHz caused by terrain echoes. The

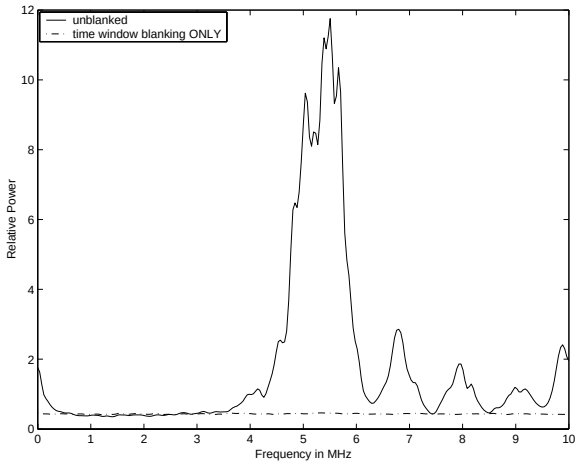


Fig. 5. The unblanked and time window blanked spectra integrated over 1.2 seconds while the RADAR beam was sweep overhead at the GBT.

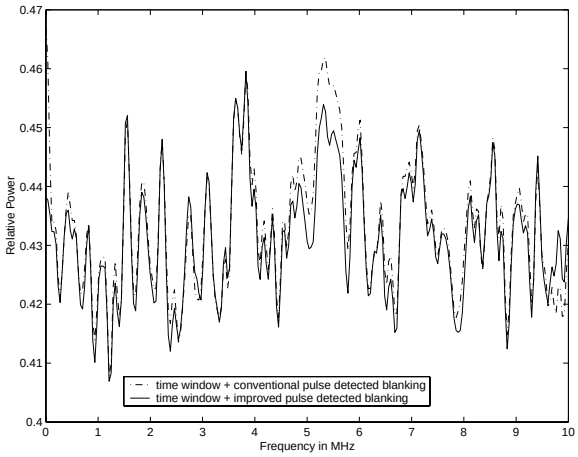


Fig. 6. The spectra with simple time window blanking combined with detected pulse blanking (using new and conventional echo detection algorithms, respectively).

spectrum with simple time window blanking is also shown, and at this scale RFI appears to have been eliminated.

However, at the expanded scale of Figure 6, a difference is seen between spectral estimates using the new Bayesian detection as compared with conventional detection. In this particular data window there were no strong aircraft echoes so there is little difference between time window blanking and conventional detected pulse blanking. There are three weak aircraft echoes which were detected with the new algorithm, and the resulting spectrum shows reduced bias near 5.5 MHz corresponding to the RADAR pulse center frequency.

Detected pulse blanking using Kalman filter tracking techniques has been shown to reduce RFI bias due to RADAR pulses in GBT observations. Also, the new Bayesian combined tracking and detection algorithm has been shown to improve blanking of weak aircraft echo pulses.

## REFERENCES

[1] Q. Zhang, Y. Zheng, S. Wilson, J. Fisher, and R. Bradley, "Combating pulsed radar interference in radio astronomy," *The Astronomical Journal*, vol. 126, pp. 1588–1594, 2003.

[2] J. Fisher, "Summary of rfi data samples at green bank," National Radio Astronomy Observatory, Green Bank Observatory, Tech. Rep., 2001.

[3] ——, "Analysis of radar data from february 6, 2001," National Radio Astronomy Observatory, Green Bank Observatory, Tech. Rep., 2001.

[4] S. Ellingson and G. Hampson, "Mitigation of radar interfernece in l-band radio astronomy," *The Astrophysical Journal Suplement Series*, vol. 147, pp. 167–176, 2003.

[5] ——, "Rfi and asynchronous pulse blanking in the 1230-1375 mhz band at arecibo," Ohio State University, Tech. Rep., 2002.

[6] P. Ravier and R. Weber, "Robustness in rfi detection for time-blanking," LESI and ESPEO, University of Orlans, France, Tech. Rep., 2000.

[7] A. Leshem and A.-J. v.d. Veen, "Introduction to interference mitigation techniques in radio astronomy," in *Perspectives in Radio Astronomy, Technologies for Large Antenna Arrays*, A. Smolders and M. van Haarlem, Eds. Dwingeloo, The Netherlands: NFRA, 1999.

[8] A. Boonstra, A. Leshem, A.-J. van der Veen, A. Kokkeler, and G. Schoonderbeek, "The effect of blanking of tdma interference on radio-astronomical observations: experimental results," in *Proc. of the IEEE International Conf. on Acoust,, Speech, and Signal Processing*, vol. 6, 2000, pp. 3546–3549.

[9] A. Leshem, A.-J. v.d. Veen, and E. Deprettere, "Detection and blanking of gsm interference in radio-astronomical observations," in *Proceedings of the 2nd IEEE Workshop on Signal Processing Advances in Wireless Communications*, 1999, pp. 374–377.

[10] K.V.Ramachandra, *Kalman Filtering Techniques for Radar Tracking*. Marcel Dekker, 2000.

[11] P. Zarchan and H. Musoff, "Fundamentals of kalman filtering: A practical approach," *Progressin Astronautics and Aeronautics*, vol. 190, pp. 257–291, 2000.

[12] B. Mahafza, *Radar Systems Analysis and Design Using MATLAB*. Chapman and Hall/CRC Press, 2000.

[13] J. Högbom, "Aperture synthesis with a nonregular distribution of interferometer baselines," *Astronomy and Astrophysics Supplement*, vol. 15, p. 417, 1974.

[14] W. Dong, "Time blanking for gbt data with radar rfi," Master's thesis, Brigham Young University, 2004.